University of Groningen

A novel method to bracket the corotation radius in galaxy discs

Roca-Fàbrega, Santi; Antoja, Teresa; Figueras, Francesca; Valenzuela, Octavio; Romero-Gómez, Mercè; Pichardo, Bárbara

IMPORTANT NOTE: You are advised to consult the publisher's version (publisher's PDF) if you wish to cite from it. Please check the document version below.

Document Version
Publisher's PDF, also known as Version of record

[Link to publication in University of Groningen/UMCG research database](#)

Citation for published version (APA):
Roca-Fàbrega, S., Antoja, T., Figueras, F., Valenzuela, O., Romero-Gómez, M., & Pichardo, B. (2014). A novel method to bracket the corotation radius in galaxy discs: vertex deviation maps. *Monthly Notices of the Royal Astronomical Society*, *440*, 1950-1963. https://doi.org/10.1093/mnras/stu437

A novel method to bracket the corotation radius in galaxy discs: vertex deviation maps

Santi Roca-Fàbrega,[1][*] Teresa Antoja,[2,3] Francesca Figueras,[1] Octavio Valenzuela,[4] Mercè Romero-Gómez[1] and Bárbara Pichardo[4]

[1]*Departament d'Astronomia i Meteorologia and IEEC-UB, Institut de Ciències del Cosmos de la Universitat de Barcelona, Martí i Franquès, 1, E-08028 Barcelona, Spain*
[2]*Kapteyn Astronomical Institute, University of Groningen, PO Box 800, NL-9700 AV Groningen, the Netherlands*
[3]*Research and Scientific Support Office, European Space Agency (ESA-ESTEC), PO Box 299, NL-2200 AG Noordwijk, the Netherlands*
[4]*Instituto de Astronomía, Universidad Nacional Autónoma de México, Ciudad Universitaria, A.P. 70-264, 04510 México, D.F., Mexico*

ABSTRACT

We map the kinematics of stars in simulated galaxy discs with spiral arms using the velocity ellipsoid vertex deviation (l_v). We use test particle simulations, and for the first time, fully self-consistent high-resolution *N*-body models. We compare our maps with the tight winding approximation model analytical predictions. We see that for all barred models, spiral arms rotate closely to a rigid body manner and the vertex deviation values correlate with the density peak's position bounded by overdense and underdense regions. In such cases, vertex deviation sign changes from negative to positive when crossing the spiral arms in the direction of disc rotation, in regions where the spiral arms are in between corotation radius (CR) and the Outer Lindblad Resonance (OLR). By contrast, when the arm sections are inside the CR and outside the OLR, l_v changes from negative to positive. We propose that measurements of the vertex deviation's pattern can be used to trace the position of the main resonances of the spiral arms. We propose that this technique might exploit future data from *Gaia* and APO Galactic Evolution Experiment (APOGEE) surveys. For unbarred *N*-body simulations with spiral arms corotating with disc material at all radii, our analysis suggests that no clear correlation exists between l_v and density structures.

Key words: methods: analytical – methods: numerical – galaxies: kinematics and dynamics – galaxies: structure.

1 INTRODUCTION

It is well known both from simulations and observations that the large-scale structures in galaxies such as bars and spiral arms strongly affect the stellar kinematics of their discs. One of the properties of such structures that is most relevant for the disc dynamics is their pattern speed which sets the position of the resonance radius. Rautiainen, Salo & Laurikainen (2008) have exhaustively reviewed the methods usually applied to external galaxies to derive this information. Some of these methods are model-independent techniques such as the so-called Tremaine & Weinberg (1984) method, whereas others are parametric – they fit several given analytical potential components to observations (i.e. Zhang & Buta 2007) – or based on the relation of various morphological or photometric features with resonances (e.g. Martínez-García, González-Lópezlira & Bruzual 2009). The model-dependent methods are based on several assumptions, the adoption of a model for the spiral arm kinematics being one of the most critical (the density wave theory is usually imposed). In addition to these methods, and thanks to the new detectors available, kinematic methods based on the analysis of the residual pattern in the velocity field have been used by Canzian (1993) and recently by Font et al. (2011). With these methods, a residual velocity map allows the exploration of the resonant structure of the galactic discs but, again, they require the removal of circular velocities (previous knowledge of the galactic rotation curve) and, up to now they have been applied only to the gas component.

Focusing in our Milky Way galactic disc, the corotation radius (CR) of the spiral pattern is still a controversial parameter. Without intending to be exhaustive, CR has been estimated, for example, by applying techniques such as the Ogorodnikov-Milne model to the Local Stellar System Kinematics of young *Hipparcos* stars (Fernández, Figueras & Torra 2001) or by evaluating the change of the kinematic substructures of the velocity field (usually named as moving groups) in test particle simulations (e.g. Chakrabarty 2007; Antoja et al. 2011). Related to this, the distribution of the fine structure in the velocity space has been used to study bars and spiral arm morphology and dynamics both from solar neighbourhood

[*]E-mail: sroca@am.ub.es

observational data (e.g. Dehnen 2000) and from more extended RAVE data (Antoja et al. 2014). All these methods require, again, the adoption of a model for the bar or spiral arm potential.

At the eve of the *Gaia* era, new methodologies have to be set up for such analysis in our Galaxy. Our aim here is to analyse deeply the connection between resonant radius and the moments of the stellar velocity distribution function. This link will open up new avenues for a model-independent kinematic method to determine CR. In this context, Vorobyov & Theis (2006, 2008) demonstrated, from simulations, how second-order moments of the stellar velocity distribution can be potential tracers of large-scale structures such as the spiral arms in galactic discs. As known, the velocity ellipsoid in axisymmetric systems is oriented with the radial and azimuthal axis of the galaxy. The misalignment of this ellipsoid, known as vertex deviation (l_v), provides important information on the non-axisymmetric components. Following that pioneer work, in this first paper, we will focus on the analysis of the l_v all through the galactic disc, postponing for further investigations the use of higher order moments or even the reanalysis of first-order moments, that is, the mean residual velocities.

The misalignment of the velocity ellipsoid in the solar neighbourhood was initially reported by Strömberg (1946). The determinations of the local l_v from *Hipparcos* data are around 30° for early-type stars and 10° for old-disc stars (Dehnen & Binney 1998). More recent measurements give values around 20°, using late-type stars from SDSS (Fuchs et al. 2009). Several possible causes for this non-null l_v have been proposed, most of them related, as mentioned, to the non-axisymmetric components (bar and spirals). These non-axisymmetric components can create patterns in the velocity field that change the shape and orientation of the velocity ellipsoid. Furthermore, the existence of fine kinematic substructure (moving groups) may also change the moments of the velocity distribution function (Binney & Tremaine 2008). This kinematic substructure can consist of groups of young stars still following similar orbits from the time when they were born or can be caused by the resonances of the non-axisymmetries of the Galaxy for example through mechanisms such as resonant trapping or scattering (Antoja et al. 2009, e.g.).

The possible connection of l_v with the spiral structure was earlier discussed by Woolley (1970) and Mayor (1970). The former concluded that l_v is a remnant of the conditions of stars when they were formed, mostly based on the fact that l_v is observed in young stars but not so clearly in the old populations. The latter used the analytical expressions of the density wave theory from Lin, Yuan & Shu (1969) to quantify this effect in the solar neighbourhood. He derived analytically the second-order moments of the velocity distribution function by considering a Galactic system composed of an axisymmetric part and a spiral perturbation and using the zero- and first-order moments computed by Lin et al. (1969). In particular, the tight winding approximation (TWA hereafter) was imposed. As described by Binney & Tremaine (2008), the TWA spiral arm model is the result of using the WKB approximation used in quantum mechanics. In Mayor (1970), the epicyclic approximation was adopted and velocity dispersions were assumed to be small (valid for a young and cool population). Furthermore, his analytical approach required a small amplitude and pitch angle of the spiral pattern (i.e. the TWA shall be fulfilled). Later on, Hilton & Bash (1982) reproduced the observed l_v sign and magnitude for young stars with a model where dense molecular clouds are launched from spiral arms at post-shock velocities, and as a consequence, the forming stars move at the same velocities. Coming back to the analytical approach, Kuijken & Tremaine (1994) found how

elliptical potentials could also lead to a non-vanishing l_v and tested their results using orbital integrations. Muhlbauer & Dehnen (2003) and Monari, Antoja & Helmi (2013) showed that a barred potential induces different l_v, depending on the position with respect to the bar and its main resonances. They also found that the l_v increases with decreasing velocity dispersion.

As discussed above, Vorobyov & Theis (2006, 2008) computed the moments of the velocity distribution function across the disc in both test particle simulations, imposing a spiral arm potential, and in spiral arm semi-analytical models (with the so-called BEADS-2D code). In this study, they found a clear correlation between the position of the density structures (i.e. the spiral arms) and the change of the sign of the l_v. They saw that large regions with positive l_v are present in front of the spiral arm (following the spiral rotation), while negative l_v were found behind the arms. In their analysis, however, only cases where the spiral structure is located outside CR were considered.

Here, we map the l_v caused by the spiral arms in the whole galactic disc. To undertake our study, we use (i) an analytical approach, (ii) test particle simulations imposing a fixed two-armed galactic potential or a bar and (iii) self-consistent *N*-body simulations. First, in our analytical development, we extend the modelling of Mayor (1970) to analyse the expression for the l_v in the TWA model not only locally, as he did, but across the whole disc. Secondly, the use of test particle simulations allows us to control the parameters of the imposed potential and to explore the parameter space and its influence on the results. For example, we can fix the position of the spiral pattern resonances at our convenience and monitor the behaviour of the l_v inside or beyond CR, which was not addressed in previous studies. Besides, we also use simulations where the spiral arms are formed as a response to an imposed barred potential. Finally, *N*-body simulations, used here for the first time to map the l_v, provide a more realistic framework because they are fully self-consistent. These simulations also allow us to analyse the evolution in time of l_v.

In Section 2, we give the definition of the l_v and the expressions to compute its error. In Section 3, we present our analytical approach and the simulations analysed here for both test particle and *N*-body simulations. The results from our analysis are presented in Section 4, and in Section 5 we summarize and give our conclusions. Finally, in Appendix A, we detail the calculations for the analytical expression of the l_v in an axisymmetric potential plus TWA spiral arms.

2 VERTEX DEVIATION

The velocity dispersion tensor that defines the (p, q, r)th centred moments of the velocity distribution at position $\boldsymbol{x}$ and time t is defined as

$$\mu_{pqr} = \frac{1}{\mu_{000}} \int \mathrm{d}^3 \boldsymbol{v} \, (u - \bar{u})^p \, (v - \bar{v})^q \, (w - \bar{w})^r \, f, \qquad (1)$$

with $\boldsymbol{v} = (u, v, w)$, where u, v and w denote, respectively, the radial, azimuthal and vertical velocity components, and $f = f(\boldsymbol{x}, \boldsymbol{v}, t)$ is the velocity distribution function. The vertex deviation (l_v) is the angle that measures the tilt of the velocity ellipsoid, in the u–v plane, compared to the orientation of an axisymmetric configuration; it is related to a non-null value of the cross-correlation coefficient μ_{110}. Here, we use the extended definition presented in Vorobyov & Theis (2006) that includes the possibility of having large l_v, which happens when breaking the epicyclic approximation locally in regions where

the spiral gravitational potential is strong:

$$\tilde{l}_v = \frac{1}{2} \text{atan} \left(\frac{2\mu_{110}}{\mu_{200} - \mu_{020}} \right) \tag{2}$$

$$l_v = \begin{cases} \tilde{l}_v & \text{if } \mu_{200} > \mu_{020}. \\ \tilde{l}_v + \text{sign}\,(\mu_{110})\,\frac{\pi}{2} & \text{if } \mu_{200} < \mu_{020}. \end{cases} \tag{3}$$

We computed the error on l_v (denoted by ϵ_{l_v}) as the propagation of the errors in the second- and fourth-order moments (Nunez & Torra 1982):

$$\epsilon_{l_v} = \left| a_4 \sqrt{ b_1 + a_1 b_2 + b_3 \left[\frac{\mu_{220}}{N} + \mu_{110}^2 a_2 + \mu_{200}\mu_{020} a_3 \right] } \right|$$

$$a_1 = 2\,(N-1)^{-1} - 3N^{-1}$$
$$a_2 = (N-1)^{-1} - 2N^{-1}$$
$$a_3 = (N-1)^{-1} - N^{-1}$$
$$a_4 = (\mu_{110}\,(a_1+4))^{-1}$$
$$b_1 = (\mu_{400} + \mu_{040})\,N^{-1}$$
$$b_2 = (\mu_{200}^2 + \mu_{020}^2)$$
$$b_3 = (\mu_{200} - \mu_{020})^2\,(\mu_{110})^{-2}. \tag{4}$$

This expression takes into account the fact that the error is larger both when the number of particles is low – due to Poisson noise – and when the velocity ellipsoid is nearly circular, so the major axis of the velocity ellipsoid is not well defined.

3 METHODOLOGY

Here, we present our analytical development as well as the characteristics of the simulations used in our analysis.

3.1 TWA analytical approach

We have derived the analytical expression for the vertex deviation $l_v(r, \theta)$ of the velocity distribution function proposed by Lin et al. (1969). This consists of a perturbed classical Schwarzschild distribution, where the perturbation is the result of an m-armed Lin & Shu (1964) spiral arm. The final expressions and the development procedure are presented in Appendix A, and they are a generalization of the expressions by Mayor (1970). We use these expressions to map the l_v values across the whole galactic disc.

As input parameters, we used a spiral arms' rotation frequency of 35 km s^{-1} kpc^{-1}, a pitch angle of 8°, a mass of 5 per cent of the disc mass, a radial velocity dispersion of 20 km s^{-1}, constant with radius, and a disc rotation curve derived from the axisymmetric Galactic model of Allen & Santillan (1991). The CR in this model is placed at 6.2 kpc and the Outer Lindblad Resonance (OLR) at 10.2 kpc, while the Inner Lindblad Resonance (ILR) does not exist. The amplitude of the spiral arms potential declines in radius as $\propto r \exp(-r/R_\Sigma)$ with a radial scalelength of $R_\Sigma = 2.5$ kpc. We use an amplitude normalization ($A_{\rm sp}$) of 850 km^2 s^{-2} kpc^{-1}. The locus of the spiral is an $m = 2$ logarithm that starts at 2.6 kpc.

3.2 Test particle simulations

We run test particle simulations using several galactic potentials. Potentials used here are the result of a superposition of an axisymmetric part plus spiral arms or bar components. In all cases, the axisymmetric component is the one described in Allen & Santillan (1991) and consists of the superposition of analytical and time-independent bulge, disc and halo potentials. Here, we analyse

Table 1. Parameters of test particle and N-body simulations. TWA, PER and FBar are test particle models with imposed cosine spiral arms, PERLAS spiral arms and Fbar, respectively (see Section 3.2). B5 and U5 are two snapshots from different N-body simulations (see Section 3.3). The i values refer to the pitch angle of the imposed spiral structure, Ω_b the pattern speed of the perturbation, $R_{\rm CR}$ its CR and $t_{\rm int}$ the integration time of the simulation.

Model	i (°)	Initial conditions	N (10^6)	Ω_b (km s^{-1} kpc^{-1})	$R_{\rm CR}$ (kpc)	$t_{\rm int}$
TWA1	8	ICMN20	5	20	10.2	5 rot.
TWA2	8	ICMN20	5	35	6.2	5 rot.
TWA3	8	ICMN20	5	50	4.04	5 rot.
PER1	8	ICMN20	4.3	35	6.2	5 rot.
PER2	15.5	IC2	4.8	20	10.2	5 rot.
FBar	–	ICMN30	80	50	4.04	18 rot.
B5	–	–	5	22	7.7	1.2 Gyr
U5	–	–	5	–	–	1 Gyr

separately the non-axisymmetric components of the potential (imposed bar and imposed spirals) to avoid a more complex scenario when interpreting the connection of density structures with the l_v.

The parameters of our basic models and characteristics of our simulations are presented in Table 1, where we show for each model some of the main properties of the potential, the number of particles and the total integration time. The number of particles in all cases is around or much higher than 5×10^6 and the integration time was from about 5 to 20 rotations of the non-axisymmetric structure. Whereas with large integration times the test particles have reached approximately total statistical equilibrium with the galactic potential, for shorter times the particles may not be completely relaxed or face-mixed. Nonetheless, by analysing snapshots with higher and lower evolution times, we tested that results presented in Section 4 are independent of the integration time.

3.2.1 Spiral arm potentials

We use two different types of spiral arm potentials, namely the TWA (Lin et al. 1969; Binney & Tremaine 2008) and the PERLAS (Pichardo et al. 2003) models, which are both described in Antoja et al. (2011). These simulations are for 2D discs. As initial conditions, we used an axisymmetric Miyamoto–Nagai disc density profile. The initial velocity field has been approximated using the moments of the collisionless Boltzmann equation, simplified by the epicyclic approximation with a local normalization of $\sigma_u(R_\odot) = 20$ km s^{-1} (for more details see Antoja et al. 2011). According to Aumer & Binney (2009), this value corresponds to a young population of late B- and early A-type stars. We refer to these initial conditions as ICMN20. In some cases, we use simulations generated for other purposes (see Antoja et al. 2011). They use an initial 2D exponential density distribution as in Hernquist (1993), and are named IC2.

The simulations named TWA1, TWA2 and TWA3 are our basic models. The non-axisymmetric component of the potential has been introduced abruptly from the beginning. Particles have been then integrated during five spiral arm rotations. We also produced experiments increasing adiabatically the spiral arms, and we noticed that for the pitch angle and spiral arms mass ratio employed here, the effect of introducing the arms impulsively (from $t = 0$) or adiabatically is negligible. The parameters that fix the TWA potential are the amplitude of the cosine perturbation $A(R) = -A_{\rm sp} R \exp(-R/R_\Sigma)$, the radial scalelength R_Σ, the number of spiral arms m, its initial phase ϕ_0, its locus $g(r)$, which in turn depends on the pitch angle i,

and the radius at which the spiral arms begin R_{sp} (see Antoja et al. 2011). Here, we used $A_{sp} = 850$ km^2 s^{-2} kpc^{-1}, $R_{\Sigma} = 2.5$ kpc, $m = 2$, $\phi_0 = 0$, $R_{sp} = 2.5$ kpc and $g(r) = -2/\tan(i)\ln(r/R_{sp}) + \phi_0$. The pattern speed for TWA1 (TWA2 and TWA3, respectively) is fixed to 20, (35 and 50, respectively) km s^{-1} kpc^{-1}, and it is assumed to be constant at all radii. As known, a change on this parameter directly produces a change in the CR. This lets us study differences in the l_v values inside or outside CR. Note that TWA2 has very similar parameters to the ones set in our analytical approach of Section 3.1.

Apart from the main models (TWA1, TWA2 and TWA3), we performed several more simulations only changing one of the parameter each time. This is to test the independence of our results on the most critical parameters: spirals amplitude, pitch angle, initial velocity dispersions of the test particles, angular speed of the pattern and total integration time.

In particular, we scanned the values of 8–15° for the pitch angle, 600–1300 km^2 s^{-2} kpc^{-1} for the TWA amplitude, 10–40 km s^{-1} kpc^{-1} for the radial velocity dispersions and 2–7 spiral rotations for the integration time.

The PERLAS model is a density distribution-based potential for the spiral arms. In this case, unlike the very simple spiral arm mathematical approximation represented by the TWA model, PER-LAS is formed, like bricks in a building, by inhomogeneous oblate spheroids, simulating beads on a necklace (from there the acronym). This model presents more abrupt gravitational potential and forces (see figs 7 and 8 in Antoja et al. 2011). We run two PERLAS models. Model PER1 has a set of parameters selected so that the spiral arms are comparable to TWA2 in terms of pitch angle (8°) and pattern speed (35 km s^{-1} kpc^{-1}). However, they produce a smaller force. This can be quantified with the parameter $Q_t(R)$ which measures the maximum azimuthal force in a given radius scaled to the axisymmetric force at that radius. While at a characteristic radius of 8 kpc this parameter is 0.005 for PER1, it is 0.017 for TWA1, TWA2 and TWA3. For model PER2, we used the same initial parameters as in PER1 but a pitch angle of 15°.5, instead of 8°, and the pattern speed is fixed to 20 km s^{-1} kpc^{-1}. Because of the larger pitch angle, the torque produced by PER2 is higher than for PER1, and it has a parameter Q_t at 8 kpc of 0.020, which makes it more similar in terms of force to the previous TWA models.

3.2.2 Barred potentials

We selected barred potentials that generate a spiral arm structure as a response. Several tests have been performed using Ferrers and quadrupole bars. As initial conditions, we used a 3D axisymmetric Miyamoto–Nagai density profile with a radial velocity dispersion at the Sun's position of $\sigma_u(R_\odot) = 30$ km s^{-1} and a scaleheight value of $h_z = 300$ pc. According to Binney & Tremaine (2008) and Robin & Creze (1986), these values would correspond to a hot population of red clump K giants. We refer to this set of initial conditions as ICMN30.

The characteristics of the bar potential presented here [Ferrers bar potential (FBar)] can be found in Romero-Gómez et al. (2011). As this model has been developed to be compared with the Milky Way, its main parameters are fixed within observational ranges for the Milky Way bar (see Romero-Gómez et al. 2011). The model is a superposition of two bars in order to obtain a boxy/bulge type of bar. For the *COBE*/DIRBE bulge, we set the semimajor axis to $a = 3.13$ kpc and the axes ratios to $b/a = 0.4$ and $c/a = 0.29$. The mass is $M_{bul} = 6.3 \times 10^9$ M$_\odot$. The length of the other bar, that is, a long bar, is set to $a = 4.5$ kpc and the axes ratios to $b/a = 0.15$ and $c/a = 0.026$. The mass of the bar is fixed to $M_b = 3.7 \times 10^9$ M$_\odot$. This bar is introduced adiabatically and its mass is subtracted from the one of the Allen and Santillan bulge (Romero-Gómez et al. 2011). The total mass is, therefore, $M_b = 10^{10}$ M$_\odot$. In this case, the bar rotates at a constant pattern speed of 50 km s^{-1} kpc^{-1}.

3.3 Collisionless *N*-body models

The *N*-body simulations we use are the ones presented in Roca-Fàbrega et al. (2013) as B5 and U5 models. All of them include a live disc and live halo but not a gas component (Valenzuela & Klypin 2003). B5 model has an effective number of particles of nearly 400 million, five of them in the disc. We built the model ensuring the formation of a strong bar and a bisymmetric spiral associated with it. U5 model is similar to B5 but has a heavier disc and a smaller halo, which inhibits the bar formation. As a consequence, in the U5 simulation a multi-armed structure dominates and resembles a late-type galaxy with transient high-m spiral waves. Simulations like the ones used here have been long tested to avoid numerical affects (see Valenzuela & Klypin 2003; Avila-Reese et al. 2005; Klypin et al. 2009).

Fig. 1 shows the rotation frequency of the disc particle and the spiral arm dominant mode (red dashed and red solid line, respectively), and the ILR and OLR curves (red dotted and red dot–dashed, respectively). The rotation frequency has been computed using the method described in Roca-Fàbrega et al. (2013). Basically, we find the spiral density structures using Fourier analysis and later on we
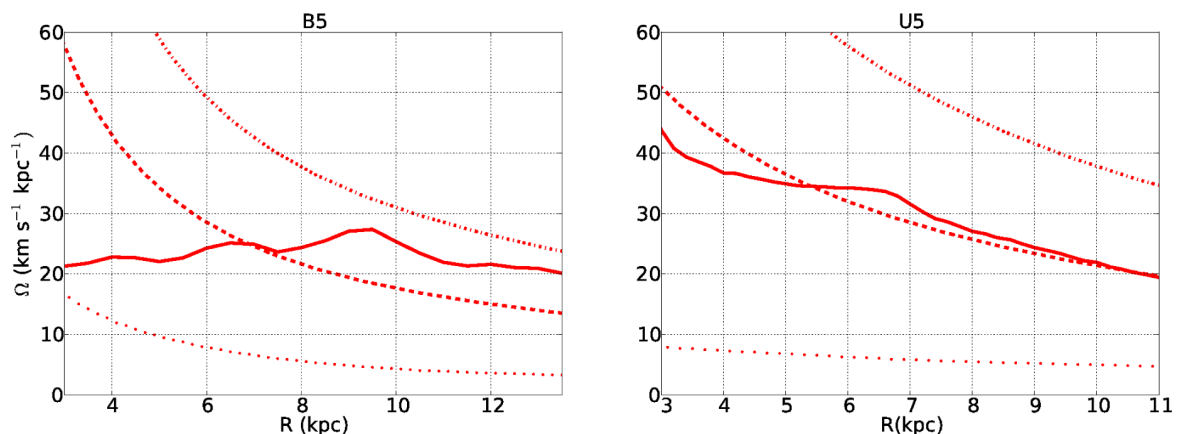

Figure 1. Disc (red dashed), and bar and spiral pattern (red solid line) rotation frequency as a function of radius for the *N*-body model B5 (left) and U5 (right). The ILR and OLR curves are shown as red dotted and red dot–dashed, respectively.

compute the rotation frequency from a finite differentiation of three consecutive snapshots of the simulation. In the B5 model, a strong bar is present up to 7.7 kpc, that is, where the spiral arm structure begins. Left-hand panel of Fig. 1 shows how the bar (that ends at CR ~ 7.7 kpc) and the spiral arms rotate at the same nearly flat rotation frequency ($\Omega = 24 \pm 3$ km s^{-1} kpc^{-1}). In the U5 model, the dominant mode is the $m = 4$ and as it can be seen in the right-hand panel of Fig. 1, spirals nearly corotate with disc particles.

The high temporal and spatial resolutions, and the large number of disc particles make U5 and B5 models one of the best available simulations to measure kinematic quantities in the entire galactic disc with enough resolution.

4 CR AND OLR RADIUS FROM VERTEX DEVIATION PATTERNS

In this section, we show the behaviour of l_v across the galactic disc in our different models. For that, we split the disc in cylindrical sectors (integrated for $|z| < 0.5$ kpc). We select each region to have a $\Delta r = 200$ pc and a $\Delta\theta = 6°$. Each region overlaps 100 pc and 3° with the contiguous ones. The expressions used for the computation of l_v and its error are given in Section 2.

In the polar plots of this section, the disc rotates from left to right. In all plots, we overplot the locus of the bisymmetric spiral structure as a thick solid black line. In the analytical analysis, this is given directly by the equation of the density perturbation of the TWA. In the simulations, we show the Fourier $m = 2$ mode locus computed by applying a spatial Fourier analysis in radial bins (Roca-Fàbrega et al. 2013). For the simulations, we also show density contours of regions with density above the mean. We computed the overdensity value of each region by subtracting the mean radial density to the local value. We mark the spiral CR with a thick solid horizontal black line and the OLR radius with a thick dashed horizontal black line, if those are well defined. Note that for U5 model there is no CR as the material is corotating with the spiral pattern and also that we do not plot the $m = 2$ Fourier mode as this does not represent the spiral structure (in this case, we have a four-armed spiral instead). The white regions in the l_v plots correspond to regions where the relative error in l_v is above 50 per cent.

4.1 TWA analytical approach

The results of our analytical development are presented in Fig. 2. This map clearly shows that l_v follows periodic patterns related to the position of the spiral arms. In particular, it changes the sign when moving from behind to in front of the spiral perturbation. Additionally, positions with maximum or minimum spiral arm potential correspond to regions with almost null l_v. This result confirms the correlation between the mass density distribution and the l_v, which was already pointed out by Vorobyov & Theis (2006).

Besides, we notice here a novel result when studying the second-order moments of the velocity distribution. We see that when crossing the spiral arm overdensity in the direction of rotation, the sign of the l_v changes from positive to negative if we are inside the CR, but the other way round between CR and OLR radius, and again from positive to negative outside the OLR radius. Note here that Mayor (1970) computed l_v values only at the solar neighbourhood in a model where the Sun was placed inside CR. Therefore, he could not notice these patterns. In next sections, we use this analytical result as a framework to understand the kinematics observed in our test particle and *N*-body simulations.
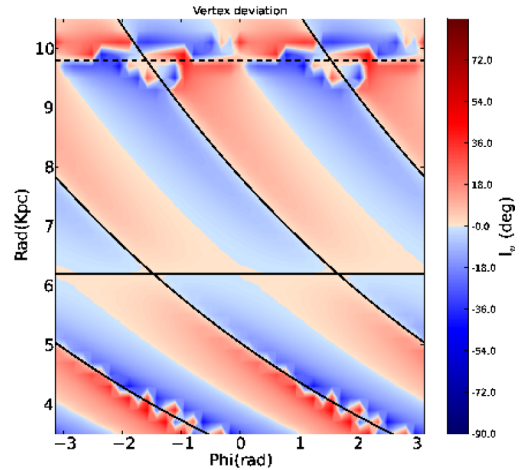

Figure 2. Vertex deviation polar plots in a colour scale (red for positive values, blue for negative) for the TWA analytical solution (see Section 3.1). The solid and the dashed horizontal black lines show the position of CR and OLR radius, respectively. The curved black solid lines show the position of the spiral arms locus. The galaxy rotates from left to right.

A question that arises from the results presented in this section is what the origin of the l_v sign changes is. We deeply analysed the analytical expression for the l_v (see equation A18) presented in Appendix to answer this question. We found that these sign changes are driven by the term $\mathrm{Re}(i\vartheta_1)D_\nu^{(1)}(x)$ in the numerator. The part $\mathrm{Re}(i\vartheta_1)$ drives the change that occurs when crossing the density peak, and it corresponds to the imaginary part of the spiral arm potential that is shifted $\pi/2$ from the spiral arm density. The term $D_\nu^{(1)}(x)$, which is a function of $\nu = m(\Omega_p - \Omega)/\kappa$, drives the change at CR and is related to the fact that the rotation frequencies of stars are larger or smaller than the patterns' rotation. This is a quantitative explanation, but a qualitative physical origin of these sign changes remains unclear.

4.2 Results from test particle models

Here, we discuss the patterns of l_v we obtained for all test particle models presented in Section 3.2 and its connection with the analytic results we show in Section 3.1.

4.2.1 TWA spiral arms potential

Fig. 3 shows the density distribution (top) and the l_v values (bottom) in polar coordinates across the whole disc for models TWA1 (left), TWA2 (middle) and TWA3 (right) that differ only by their spiral pattern rotation frequency. When we compare these plots with Fig. 2, we see that the l_v structures are not so sharp. We also see that due to both the Poisson noise and that the velocity ellipsoid is so rounded, the l_v has a large uncertainty in some regions. As explained before, these regions with a high error in the l_v appear in white.

Here, we see the same behaviour of l_v as seen in the analytical expressions of previous section. This is consistent and expected because the underlying spiral arm potential model is the TWA in both cases. However, here we did not impose a certain distribution function but computed the real orbits of particles in this potential. In particular, we can clearly see this for TWA2 which is a test particle simulation with similar initial conditions and parameters as the analytical approach potential. For the other two cases, TWA1 and TWA3, where most of the disc is either inside or outside CR,
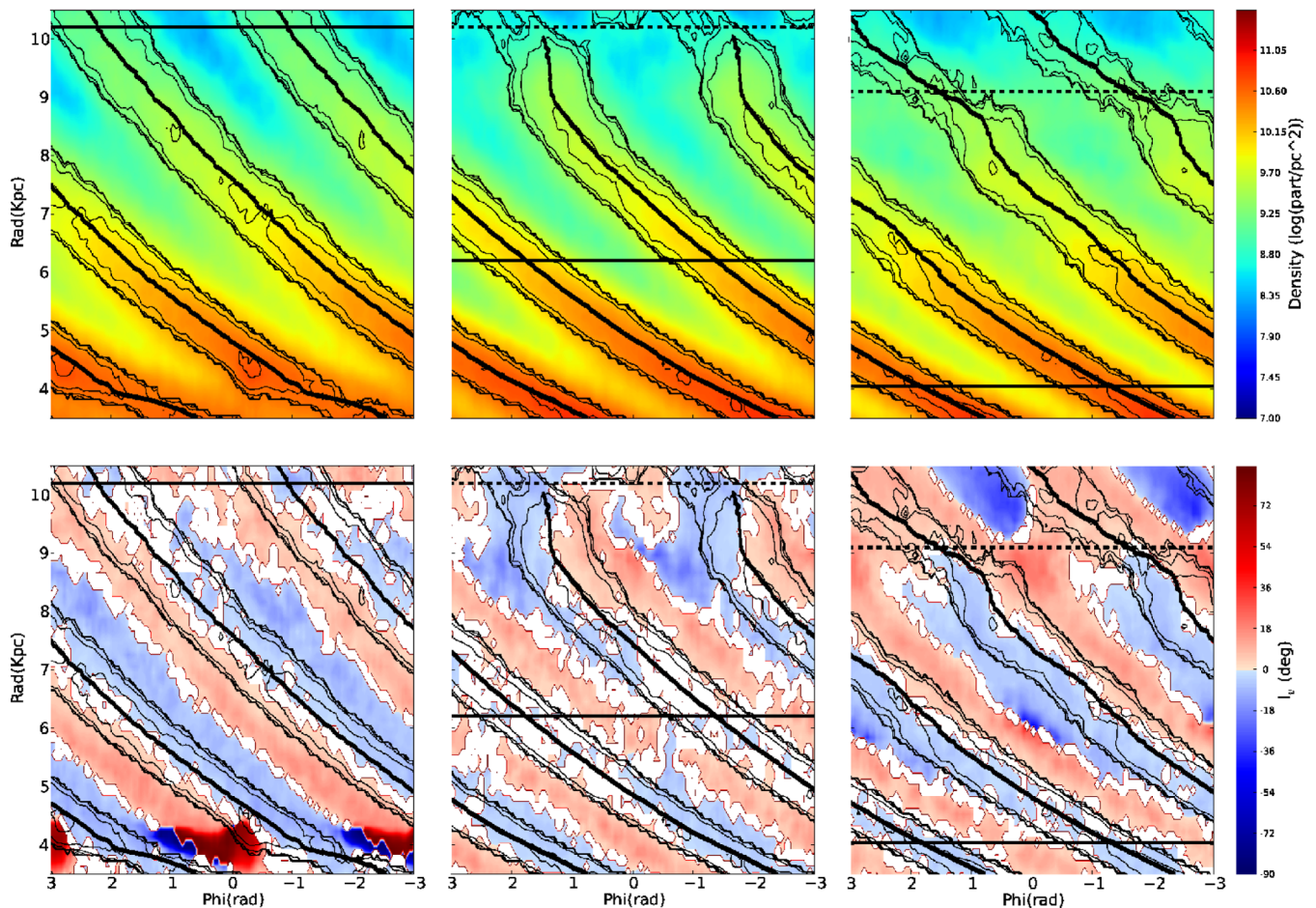
Figure 3. Density (top) and l_v (bottom) polar plots for test particle models TWA1 (left), TWA2 (middle) and TWA3 (right) from Table 1. The thin black lines show density contours of regions with density above the mean. The thick and dashed horizontal black lines show the position of CR and OLR radius, respectively. The thick black lines show the position of the Fourier $m = 2$ mode locus. The white regions at the bottom panels correspond to regions where the l_v relative error is above 50 per cent.

we observe that the behaviour is the same as inside or outside CR, respectively, in TWA2. Note also the reverse of l_v sign beyond OLR for TWA3.

To see all these results in more detail, we plot in Fig. 4 (top panels) the l_v and the overdensity (black) values, as a function of angular distance to the spiral arm overdensity peak, for the models TWA1 (left) and TWA3 (right). This distance is taken as positive in the sense of rotation. Two error bars are overplotted to the l_v points. The blue ones show the root mean square of the errors obtained from equation (4), so they reflect the Poisson noise (low number of particles) and the uncertainty when the velocity ellipsoid is almost circular. The red error bar is simply the error of the mean, that is, the standard deviation divided by the square root of the number of regions. It accounts for the spread on l_v at a given angular distance in the radial interval considered. The l_v for TWA1 follows an oscillation from negative values in front of the spiral arm (for phases 0 to $\pi/2$), through null l_v in the interarm region ($\pi/2$), to positive values when approaching the next spiral arm from behind (for phases $\pi/2$ to π). If we compare the l_v oscillation with the one of the overdensity, we can conclude that the former is shifted about $\pi/4$ towards to smaller angles. An opposite shift is observed for TWA3. Note also that a small shift is present at 0 phase: l_v is not exactly zero. This shift can be a consequence of the difficulty of finding the density peak properly as it is not a simple sharp peak.

We also point out here that TWA1 and TWA3 models show a clear antisymmetry with respect to interarm region (angular distance from the spiral equal to $\pi/2$). This is a consequence of the symmetries of the potential, similar to what happens in a barred model where there is four-fold symmetry (Fux 2001). In this case, the symmetries are related precisely to the phase with respect to the spiral arm and that is why it appears in this maps.

After our exploration of parameters detailed in Section 3.2, we conclude that the behaviour of the l_v presented here is independent of the parameters of the TWA potential and of the initial conditions. We also observe that when imposing lower velocity dispersions in the initial conditions, the l_v signatures have a better definition than when we use higher velocity dispersions.

4.2.2 PERLAS spiral arms potential

In Fig. 5, we show the density (top) and the l_v (bottom) in polar plots of the test particle models where we imposed the PERLAS spiral arm potentials PER2 (left) and PER1 (right). This potential is more complex than the cosine expression for the force of the TWA and, as a consequence, the density structures appearing in these models are more complex. One can see, for instance, a bar-like structure in the inner radius for PER1 or the two overdensities outside the spiral arms at a radius between 8 and 9 kpc for PER2.
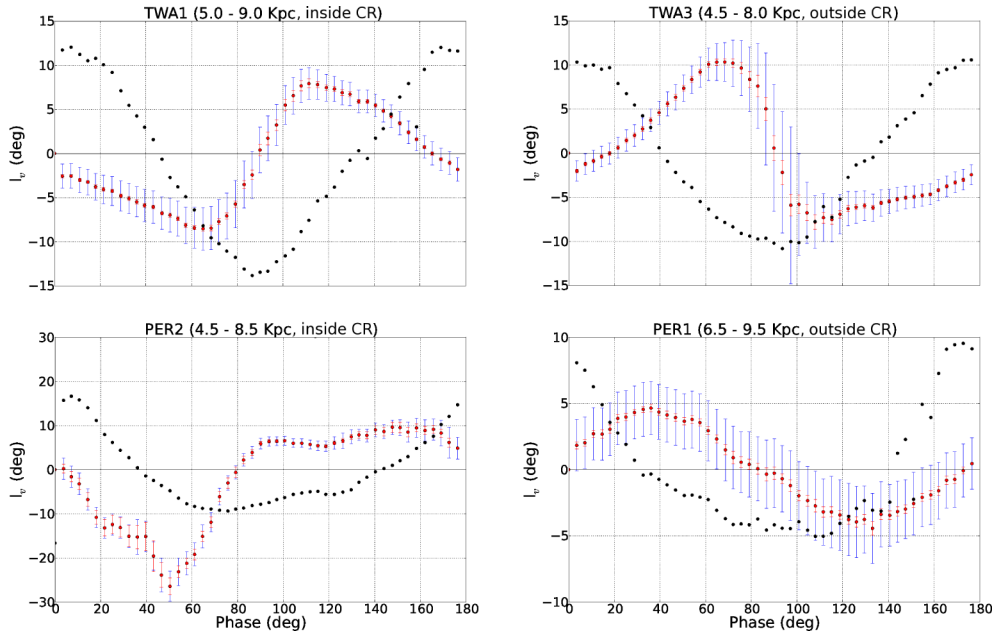
Figure 4. Vertex deviation radial mean values with their errors (blue/red error bars) and spiral arm mean overdensity with respect to the mean disc density (black points), as a function of angular distance to the spiral. The phase has been adjusted so that the spiral arm density peak is located at a phase of 0°, while the minimum is at 90°. The blue error bars correspond to the root mean square of errors computed using equation (4), and the red error bars to the error of the mean. The overdensity values have been normalized to fit in the l_v plot for a better comparison of the curves. Left: values in regions inside CR (TWA1, top, PER2, bottom). Right: regions outside CR (TWA3, top, PER1, bottom).

The l_v analysis reveals that, as in the TWA models, there is a clear relation between this parameter and the density structures. In PER1, outside CR, we observe the same l_v pattern as in TWA analytical and test particle models in the same region: positive sign in front of spirals and negative sign behind them. Inside CR, however, we do not see a clear behaviour due to the fact that the l_v values are small and that in these regions there are many density substructures. We point out that the presence of these density substructures (apart from the main imposed spiral arms) explains the higher uncertainty that exists around the CR.

For PER2, which is inside CR in the shown range of radius, in general we observe the same l_v behaviour as in the analytical solution and in the TWA models inside CR. Note, however, that between 8 and 9 kpc, where additional overdensities showed up, the l_v appears distorted. Note also that the magnitude of the l_v is much smaller for PER1 than for PER2, as corresponding to its smaller force amplitude (see Section 3.2).

The results for PER models become more clear in Fig. 4, bottom panels, where we plot l_v values as a function of angular distance to the spiral arm overdensity peak. The general behaviour of the oscillation for PER1 is similar to TWA3 (outside CR), although the magnitude of the l_v is smaller as correspond to a smaller $Q_t(R)$ (Section 4.2.2). For PER2, the oscillation resembles that of the TWA1 (inside RC) in a first approach. However, the detailed shapes of the curves of models TWA and PER are slightly different. Again, this must be due to the differences in the force fields, in particular in the shape of the forces as a function of the position in the disc mentioned in Section 3.2. Note also that a comparison between these two different models was done by Antoja et al. (2011) who concluded that, even when models with the same spiral locus, amplitude of the force and pattern speed were used, the obtained velocity field could be significantly different in some parts due to the difference in the force field. As an example, the antisymmetry in the l_v distribution observed in TWA models is clearly broken in the PER2 case. As

seen in Pichardo et al. (2003), in the PERLAS model forces are not symmetric with respect to the spiral arm locus, that is, the ones in front of the spiral are different from the ones behind.

4.2.3 Ferrers bar potential

Here, we analyse spiral arm structures that are produced as a response of a 3D bar potential. In Fig. 6, we present the density (top) and l_v (bottom) polar maps for a test particle simulation where we imposed an FBar. The spiral arms generated in this simulation can be observed in the top panel as the diagonal structures. The vertical straight structure between 3 and 4 kpc is the bar, whereas a ring-like structure is formed between 4 and 6 kpc. As a consequence of its nature, the spirals formed in these models have low amplitude and are placed outside CR.

As can be seen in Fig. 6 (bottom), the ring region presents a complicated l_v pattern. Out of it, that is at radius >7.0 kpc, the spirals created as a response of the bar are faint (low amplitude) but well defined. In Fig. 7, we present the oscillating pattern of the l_v and the overdensity induced by these spirals in the radial interval $7 < R < 9$ kpc. We observe positive vertex deviation structures in front of the spirals and negative deviation behind them, with almost null values near the locus $(0,\pi)$ and in the interarm region $(\sim \pi/2)$. This pattern is clearly shifted $\sim \pi/4$ to the density pattern. This behaviour is in agreement with the trend observed in TWA3 and PER1 models (see Fig. 4, right).

4.3 Results from *N*-body models

In these models, we have a more complex scenario as the gravitational potential has not been imposed, but it is generated by the system particles themselves. As a consequence, of this self-generation there are several density structures interacting with each other through gravity. Moreover, as discussed in Roca-Fàbrega et al.
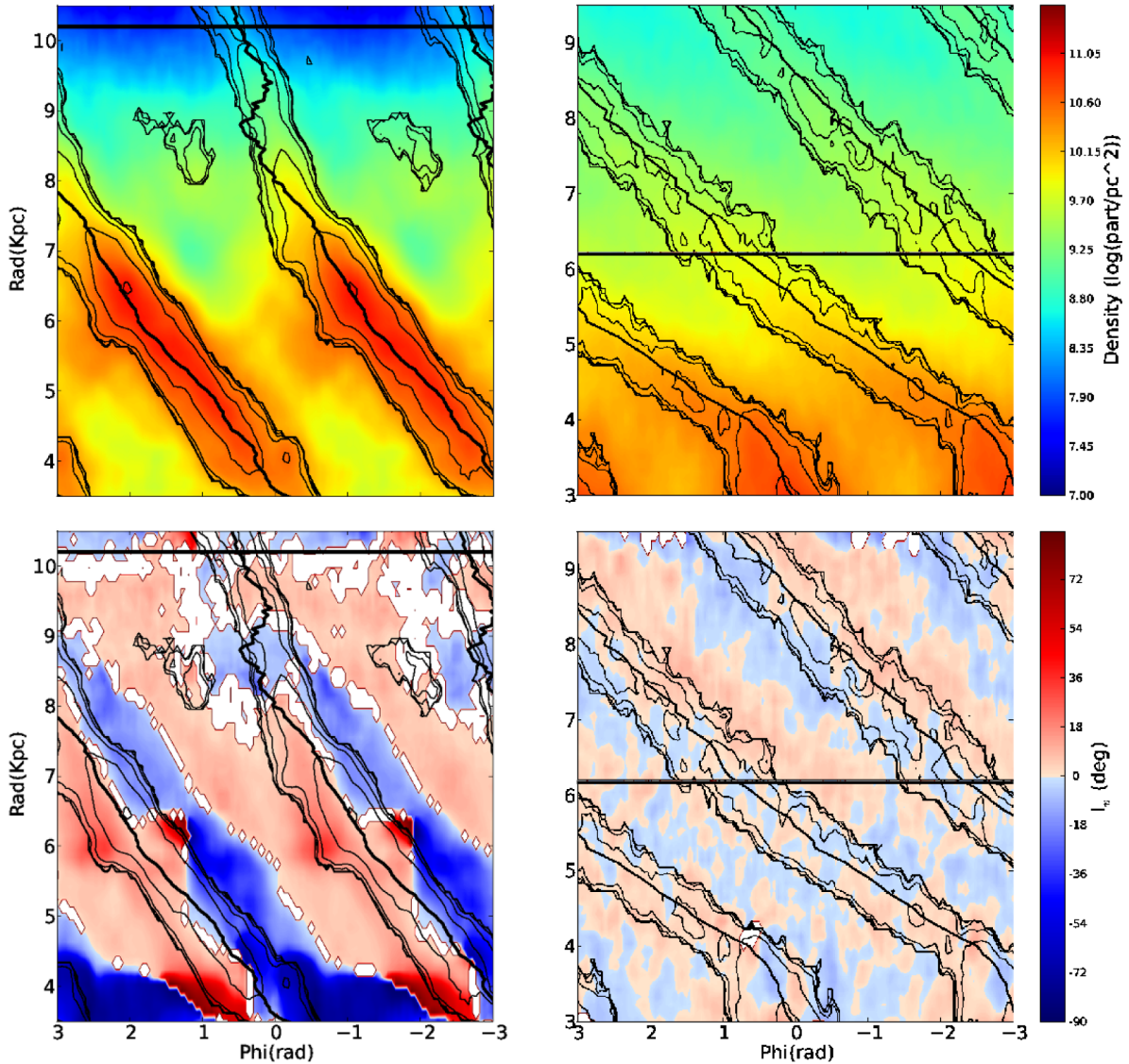
Figure 5. Density (top) and l_v (bottom) polar plots for test particle spiral arm models PER2 (left) and PER1 (right) from Table 1. See Fig. 3 for more details on the lines.

(2013), these are time-dependent structures (e.g. spiral arms are transient), which introduce an additional parameter when analysing the l_v maps.

As mentioned in Section 3.3, the B5 *N*-body simulation develops a strong bar and a dominant bisymmetric spiral arm which rotates roughly as a rigid body (see Fig. 1). The spirals in this simulation are placed outside CR. In this model, we clearly observe that, in agreement with the behaviour found in previous sections, positive values are found in front of the spiral and negative values are found behind (Fig. 8, left, and Fig. 9, top). Another interesting feature of this model is the presence of a slow rotating $m = 2$ mode at large galactic radius ($R \sim 12$–14 kpc) (see Roca-Fàbrega et al. 2013). This is seen in Fig. 8, left, where there seems to be a bifurcation in the arms at outer radius or the presence of additional arms that are not in phase with the main ones. These new arms rotate slower than the disc with a frequency of about 8 km s^{-1} kpc^{-1}, and they produce their own signature in l_v: see the additional two red regions at $\phi \sim -0.5$ and 2.5 rad, and radius of $R \sim 12.5$ kpc. These arms do show the same behaviour as previous arms inside CR, i.e. negative sign in front of the density perturbation and positive behind it.

The second model that we analyse here is the U5 simulation. This simulation develops a multiple armed system with Fourier-dominant mode being $m = 4$, without a bar, and it corotates with the disc particles. The amplitude in the density of the arms in U5 is much smaller ($A_4/A_0 \sim 0.08$) than in B5 ($A_2/A_0 \sim 0.5$). We present the results for U5 model in Figs 8, right, and 9, bottom. Although the amplitude of the l_v pattern is small in this case, the small error bars allow us to provide indications that a periodicity is also present. However, in this case, there is no clear relation between the l_v structures and density pattern. This behaviour is completely different from the B5 presented before.

Finally, we make a first attempt to analyse the evolution of the l_v behaviour when the density structures evolve in time in our *N*-body simulations.[1] We find that each density structure generates its own l_v pattern. For model B5, we see that the conclusions presented here are valid when strong spiral arms are present. Otherwise, when complex density structures appear, the relation between them and
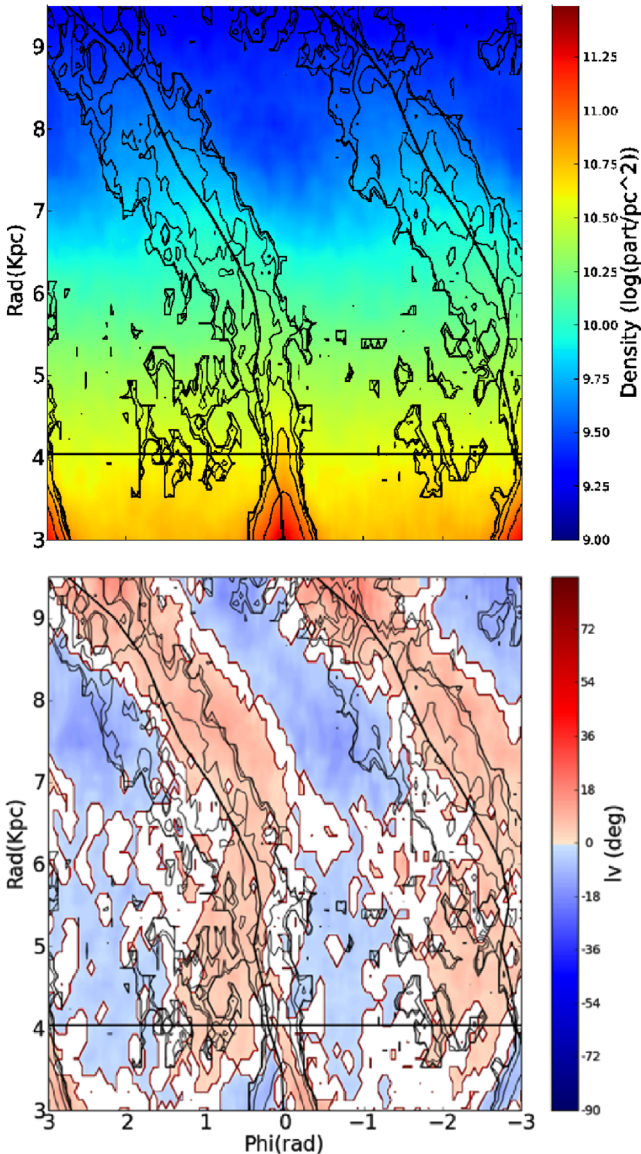
---

[1] See movies in http://www.am.ub.edu/~sroca/Nbody/movies/.

Figure 6. Density (top) and l_v (bottom) polar plots for model FBar from Table 1. See Fig. 3 for more details on the lines.
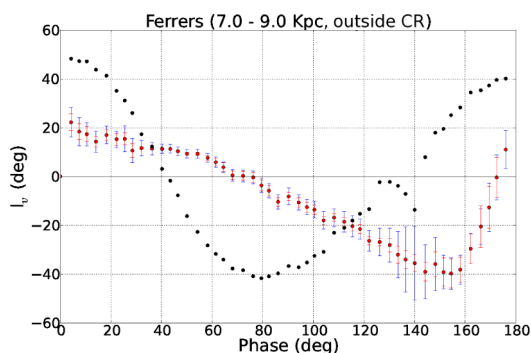

Figure 7. Vertex deviation radial mean values with their errors (blue/red points) and spiral arm overdensity (black points) as a function of distance to the spiral arms density peak, for the Ferrers bar model, i.e. outside CR. For more details see Fig. 4.

the l_v is not straightforward. The same stands for model U5, with corotating spirals.

5 CONCLUSIONS

In this paper, we analysed the l_v in simulated galactic discs with spiral structure. We mapped the l_v all across the disc using a TWA analytical solution, several test particle simulations with imposed spiral or bar potentials and, for the first time, high-resolution N-body simulations. Our main outcomes are as follows.

(i) We confirm that the l_v is clearly related to the density structure when the spiral arms are non-corotating.

(ii) In all cases with non-corotating spiral arms, the sign of the l_v changes when crossing the density peak of the spiral structure and in the interarm region. When crossing the density peak, this change is from negative to positive between CR and OLR radius and the other way round inside CR and outside OLR.

(iii) When the spiral arms are corotating, there is no clear correlation between the l_v and the overdensity.

Using test particle simulations, we have exhaustively checked that these conclusions hold both for spiral arm potential (TWA and PERLAS) and spiral arms that are the response to an imposed bar potential (Ferrers and quadrupole). Furthermore, they are independent of the initial parameters, thus of the changes of the pitch angle, the amplitude of the spirals, the velocity dispersion of the population or the total integration time. All these cases consist of a rigid rotating pattern with well-defined CR and ILR and OLR resonances. Moreover, for the first time we show here that our self-consistent high-resolution N-body simulation with a rigid rotating bisymmetric and well-defined two-armed spiral shows an l_v behaviour with the same main trends as observed in the test particle simulations.

From these models, we conclude that the changes on the sign in l_v when crossing the overdensities and underdensities of the spiral arms give us robust and useful information about the position of the main resonant radii, that is CR and OLR. Measuring the sign of the l_v in front or behind the spiral structure in a certain radius and azimuth would indicate whether that region of the galaxy is inside or outside of CR. A reverse of the sign behaviour at a certain radius would mark the CR, and in turn, give an estimation of the pattern speed of the spiral arms. As the position of spiral arms inside or outside CR is related to their nature (e.g. manifold spiral arms are generated always outside CR), the mapping of the l_v would also trace the nature of the spiral arms in a galaxy.

Second-order differences in the shape and magnitude of l_v patterns are observed when comparing all the models analysed here. These irregularities may be due to the intrinsic differences among their corresponding force fields. This is a matter that deserves further investigation, but it is out of the scope of the present study.

One may wonder why models with different nature such as the TWA (low amplitude approach), PERLAS (self-gravitating imposed potential), response spirals in test particle barred models or N-body simulations with a well-defined spiral pattern (transient structures, self-consistent model) show the same general trends for the l_v. The explanation could come from the fact that the l_v is a first-order effect of the velocity field, so its behaviour is successfully reproduced in all our models. We may require N-body simulations with a larger number of particles in order to populate the velocity distribution tails and disentangle the differences between models through higher order momenta.

Other aspects should be addressed in a forthcoming paper in order to use our proposal as a new method to find CR and OLR. First, an
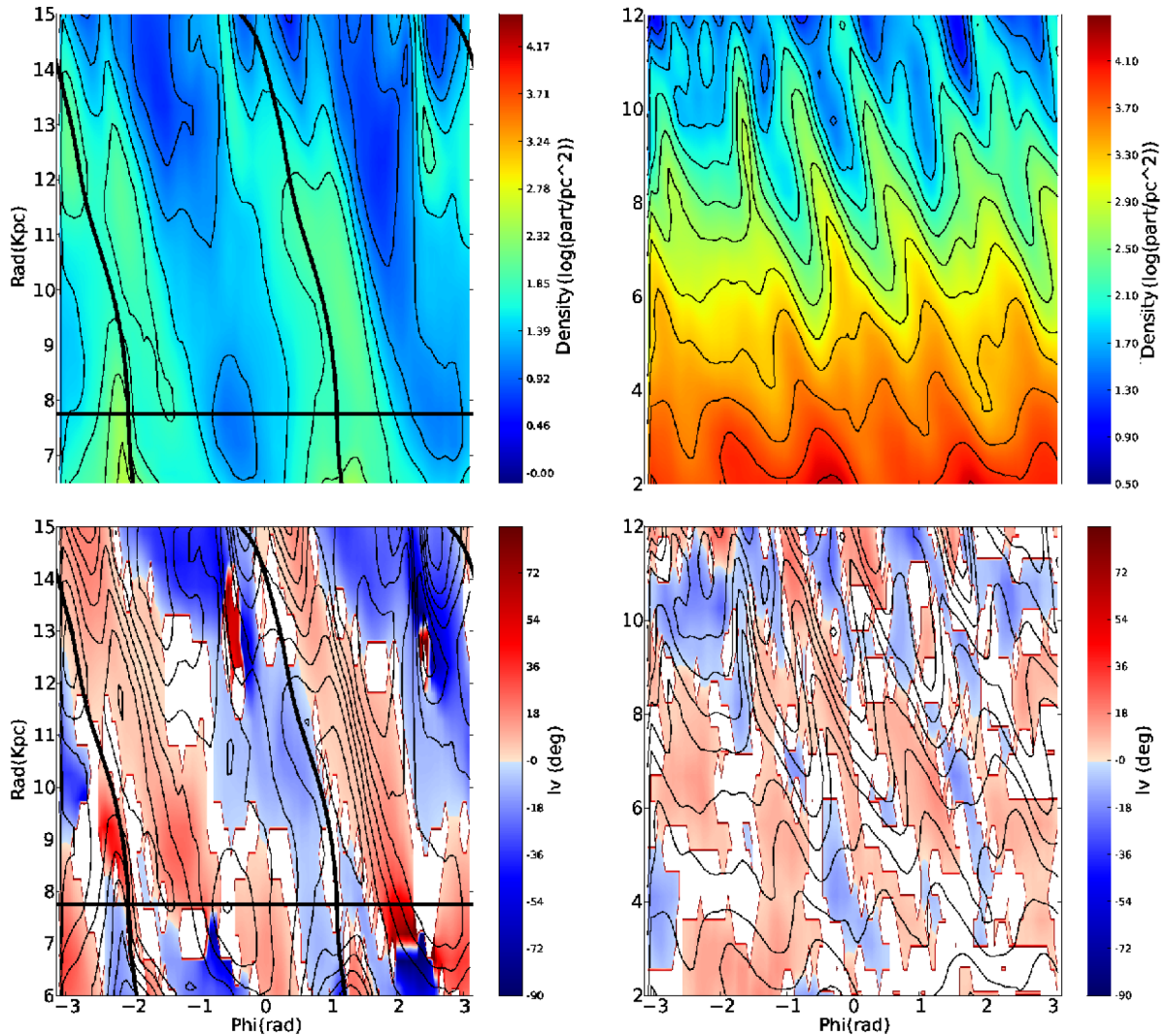
Figure 8. Density (top) and l_v (bottom) polar plots for *N*-body models B5 (left) and U5 (right) at 1.06 Gyr of evolution. See Fig. 3 for more details on the lines.

evident caveat is that the patterns in the sign of the l_v are degenerate for inside CR and outside OLR. In this case, one would need other kinematic signatures to differentiate between those two cases. Secondly, when spiral arms coexist with other density structures (i.e. rings, flocculent structures,...), the behaviour of the l_v can be much more complex. In these cases, it will be more difficult to apply the method. Finally, as it is known that the mean velocities can also be good tracers of the CR (see Binney & Tremaine 2008), it has to be studied in which cases one method is better than the other and how they can be used complementary.

In particular for our own Galaxy, where the spiral structure is one of the main debated features in Galactic studies, it is still pending if the Sun is inside or outside spirals' CR. Measurements of the l_v at several kpc from the solar neighbourhood are expected with forthcoming large surveys like *Gaia* (ESA; Perryman et al. 2001), LSST or the APO Galactic Evolution Experiment (APOGEE-SDSS; Majewski et al. 2010). The work presented here is offering new strategies to exploit this data.

For external galaxies, as far as we know, there are no measurements of the l_v. In fact, in studies of the kinematics of external galaxies, it is generally assumed that there is alignment of one of the axis of the stellar velocity ellipsoid with the azimuthal coordinate (i.e. there are no l_v) in order to derive properties such as the ratio between radial and azimuthal velocity dispersions from line of sight velocity measurements (Westfall, Bershady & Verheijen 2011; Gerssen & Shapiro Griffin 2012). Our simulations would allow one to quantify how this assumption could bias their final results. Secondly, they can be used to establish the level of detection of l_v signals in external galaxies and to study which are the observational requirements and perspectives for detecting them with current and future instruments like ELT in its spectroscopic phase or possible nanoarcsecond post-*Gaia* missions.
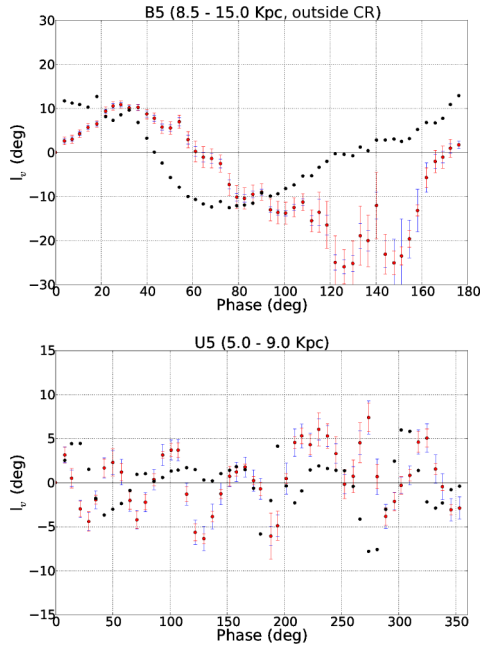
Figure 9. Vertex deviation radial mean values with their errors (blue/red points) and spiral arm overdensity (black points). For more details see Fig. 4. Top: B5 model, i.e. outside CR; values are plotted as a function of the angular distance to the spiral arm density peak. Bottom: U5 model, i.e. corotating structure; values are plotted for all the [0, 360] angular distance range, with origin at an arbitrary angle.

REFERENCES

Allen C., Santillan A., 1991, Rev. Mex. Astron. Astrofis., 22, 255
Antoja T., Valenzuela O., Pichardo B., Moreno E., Figueras F., Fernández D., 2009, ApJ, 700, 78
Antoja T., Figueras F., Romero-Gómez M., Pichardo B., Valenzuela O., Moreno E., 2011, MNRAS, 418, 1423
Antoja T. et al., 2014, A&A, 563, 60
Aumer M., Binney J. J., 2009, MNRAS, 397, 1286
Avila-Reese V., Carrillo A., Valenzuela O., Klypin A., 2005, MNRAS, 361, 997
Binney J., Tremaine S., 2008, Galactic Dynamics, 2nd edn. Princeton Univ. Press, Princeton, NJ
Canzian B., 1993, ApJ, 414, 487
Chakrabarty D., 2007, A&A, 467, 145
Dehnen W., 2000, AJ, 119, 800
Dehnen W., Binney J. J., 1998, MNRAS, 298, 387
Fernández D., Figueras F., Torra J., 2001, A&A, 372, 833
Font J., Beckman J. E., Epinat B., Fathi K., Gutiérrez L., Hernandez O., 2011, ApJ, 741, L14
Fuchs B. et al., 2009, AJ, 137, 4149
Fux R., 2001, A&A, 373, 511
Gerssen J., Shapiro Griffin K., 2012, MNRAS, 423, 2726
Hernquist L., 1993, ApJS, 86, 389
Hilton J. L., Bash R., 1982, ApJ, 255, 217
Klypin A. A., Valenzuela O., Colín P., Quinn T., 2009, MNRAS, 398, 1027
Kuijken K., Tremaine S., 1994, ApJ, 421, 178
Lin C. C., Shu F. H., 1964, ApJ, 140, 646
Lin C. C., Yuan C., Shu F. H., 1969, A&A, 155, 721
Majewski S. R., Wilson J. C., Hearty F., Schiavon R. R., Skrutskie M. F., 2010, in Cunha K., Spite M., Barbuy B., eds, Proc. IAU Symp. 265, Chemical Abundances in the Universe: Connecting First Stars to Planets. Cambridge Univ. Press, Cambridge, p. 480
Martínez-García E. E., González-Lópezlira R. A., Bruzual G., 2009, ApJ, 694, 512
Mayor M., 1970, A&A, 6, 60
Monari G., Antoja T., Helmi A., 2013, preprint (arXiv:e-prints)
Muhlbauer G., Dehnen W., 2003, A&A, 401, 975
Nunez J., Torra J., 1982, A&A, 110, 95
Perryman M. A. C. et al., 2001, A&A, 369, 339
Pichardo B., Martos M., Moreno E., Espresate J., 2003, ApJ, 582, 230
Rautiainen P., Salo H., Laurikainen E., 2008, MNRAS, 388, 1803
Robin A., Creze M., 1986, A&A, 157, 71
Roca-Fàbrega S., Valenzuela O., Figueras F., Romero-Gómez M., Velázquez H., Antoja T., Pichardo B., 2013, MNRAS, 432, 2878
Romero-Gómez M., Athanassoula E., Antoja T., Figueras F., 2011, MNRAS, 418, 1176
Strömberg G., 1946, ApJ, 104, 12
Tremaine S., Weinberg M. D., 1984, ApJ, 282, 5
Valenzuela O., Klypin A. A., 2003, MNRAS, 345, 406
Vorobyov E. I., Theis C., 2006, MNRAS, 373, 197
Vorobyov E. I., Theis C., 2008, MNRAS, 383, 817
Westfall K. B., Bershady M. A., Verheijen M. A. W., 2011, ApJS, 193, 21
Woolley R., 1970, in Becker W., Kontopoulos G. I., eds, Proc. IAU Symp. 38, The Spiral Structure of our Galaxy. Reidel, Dordrecht, p. 423
Zhang X., Buta R. J., 2007, AJ, 133, 2584

APPENDIX A: ANALYTICAL EXPRESSIONS FOR THE VERTEX DEVIATION USING THE TWA APPROACH

Here, we compute the analytical values for the vertex in the whole galactic disc plane ($z = 0$) when imposing Lin & Shu (1964) classical spiral arms. We started from the classical definition (see equation 2) and we computed up to second-order moments of the velocity distribution function. Finally, following Lin et al. (1969) we derived an expression similar to the one presented in Mayor (1970) (see equation A18).

A1 Notation

Here, we detail the notation we will use in next sections.

Ψ	$=$	Total velocity distribution function,
Ψ_0	$=$	Schwarzschild velocity distribution function,
σ_*^0	$=$	Non-perturbed surface density ($M_\odot$ kpc^{-2}),
$\sigma_\star$	$=$	Total surface density ($M_\odot$ kpc^{-2}),
$m_\star$	$=$	Stellar mass. We assume it is the same for all stars ($M_\odot$),
ϖ	$=$	Distance to the galactic centre in the disc plane (kpc),
θ	$=$	Azimuthal angle in the disc plane (rad.),
θ	$=$	Time (s),
Ω	$=$	Angular velocity of a particle in a circular orbit in the axisymmetric averaged potential of the galactic disc (km s^{-1} kpc^{-1}),
Θ	$=$	Radial velocity (km s^{-1}),
Π	$=$	Azimuthal velocity (km s^{-1}),
Z	$=$	Vertical velocity (km s^{-1}),
c_ϖ	$=$	Θ : radial residual velocity (km s^{-1}),
c_θ	$=$	$\Pi - \varpi\Omega$: azimuthal residual velocity (km s^{-1}),
c_z	$=$	Z : vertical residual velocity (km s^{-1}),
V_ϖ, V_θ	$=$	Radial and azimuthal mean systematic movements (km s^{-1}),
σ_ϖ	$=$	$\sqrt{\mu_{200}^{(0)}}$: dispersion of the non-perturbed radial residual velocities (km s^{-1}),
l_v	$=$	Vertex deviation (rad.),
κ	$=$	$2\Omega\sqrt{1 + \frac{\varpi}{2\Omega}\frac{d\Omega}{d\varpi}}$: epicyclic frequency (km s^{-1} kpc^{-1}),
γ	$=$	$\frac{2\Omega}{\kappa}$
i	$=$	Pitch angle of the spiral (rad.),
m	$=$	Number of spiral arms,
ω	$=$	Rotation frequency of the spiral (km s^{-1} kpc^{-1}),
Ω_p	$=$	Re(ω)/m Angular velocity of the spiral arm pattern (km s^{-1} kpc^{-1}),
R_0	$=$	Initial radius for the spiral perturbation (kpc),
Φ	$=$	$-\frac{2}{\tan i}\ln\left(\frac{\varpi}{R_0}\right)$: spiral arm locus,
K	$=$	$\frac{d\Phi}{d\varpi}$: Wavenumber (kpc^{-1}),
A_{sp}	$=$	Spiral arms potential amplitude normalization (km^2 s^{-2} kpc^{-1}),
R_Σ	$=$	Spiral arms radial scalelength (kpc),
A	$=$	$-A_{sp}\varpi\exp^{-\varpi/R_\Sigma}$: amplitude of the spiral arms potential (km^2 s^{-2}),
ϑ_1	$=$	$A\exp^{i(\omega t - 2\theta + \Phi(\varpi))}$: spiral arm potential (km^2 s^{-2}),
x	$=$	$K^2\frac{\sigma_\varpi^2}{\kappa^2}$: Toomre number,
ν	$=$	$\frac{m(\Omega_p - \Omega)}{\kappa}$;
V_1	$=$	$\frac{(2\Omega)(\varpi\Omega)}{\kappa}$;
a	$=$	$\frac{(K\varpi)\left(2\Omega^2\right)}{\kappa^2}$;
$\mu_0 = \frac{V_1^2}{\sigma_\varpi^2}$		
ξ	$=$	$\frac{c_\varpi}{V_1}$; $\eta = \frac{c_\theta}{\varpi\Omega}$: dimensionless velocities referred to local values,
$\langle f \rangle$	$=$	$\frac{m_*}{\sigma_*^0}\int\int\int f\Psi_0 dc_\varpi\, dc_\theta\, dc_z$: weighed average with respect to Ψ_0

A2 Velocity distribution function

To compute the moments, we used the velocity distribution function first presented in Lin et al. (1969). This function (equation A1) is a direct summation of a classical Schwarzschild distribution (Ψ_0) and a small perturbation due to the presence of a tightly wound spiral (Ψ_1). For details on the derivation of Ψ_1 see appendix A in Lin et al. (1969).

$$\Psi = \Psi_0 + \Psi_1$$
$$\Psi_0 = P_0(\varpi)\exp^{-\frac{\mu_0}{2}(\xi^2 + \eta^2)}$$
$$\Psi_1 = \frac{-\vartheta_1}{\sigma_\varpi^2}\Psi_0(1 - q),$$

where

$$q = \frac{\nu\pi}{\sin(\nu\pi)}\frac{1}{2\pi}\int_{-\pi}^{\pi}\exp^{i[\nu\alpha - a\cdot\xi\sin\alpha + a\cdot\eta(1+\cos\alpha)]}\, d\alpha \tag{A1}$$

A3 Computation of the moments

The equations presented in this section have been obtained imposing the perturbed velocity distribution function (equation A1) to the general expression for the moments, equation (1). To get the final expressions shown here, we used the relations proposed in Section A3.5 and also that the first-order moments and the crossed second-order moments of a non-perturbed Schwarzschild velocity distribution function are 0 ($\mu_{100}^{(0)} = \mu_{010}^{(0)} = \mu_{110}^{(0)} = 0$). The epicyclic approximation was used to link the second-order moments of the non-perturbed Shchwarzschild velocity distribution function ($\mu_{020}^{(0)} = \mu_{200}^{(0)}(2\Omega/\kappa)^{-2}$). A detailed example of how we obtain the final expressions can be seen in equations (A3) and (A4).

A3.1 Zero-order moments

To obtain the expressions for the zero-order moments, we used the equation (A12).

$$\sigma_*^0 = \mu_{000}^{(0)} = m_* \int\int\int \Psi_0 \mathrm{d}c_\varpi \mathrm{d}c_\theta \mathrm{d}c_z \tag{A2}$$

$$
\begin{aligned}
\sigma_* = \mu_{000} m_* &= m_* \int\int\int \Psi \mathrm{d}c_\varpi \mathrm{d}c_\theta \mathrm{d}c_z = m_* \int\int\int \Psi_0 + \Psi_0 \frac{-\vartheta_1}{\sigma_\varpi^2}(1-q)\mathrm{d}c_\varpi \mathrm{d}c_\theta \mathrm{d}c_z \\
&= \sigma_*^0 \left(1 - \frac{\vartheta_1}{\sigma_\varpi^2}\langle(1-q)\rangle\right) = \sigma_*^0 \left[1 - \frac{\vartheta_1}{\sigma_\varpi^2}\left(1 - \frac{\nu\pi}{\sin(\nu\pi)}\frac{1}{2\pi}\int_{-\pi}^{\pi}\cos(\nu\alpha)\exp^{-\frac{a^2}{\mu_0}(1+\cos\alpha)}\mathrm{d}\alpha\right)\right]
\end{aligned}
\tag{A3}
$$

A3.2 First-order moments

We obtained the expressions for the first-order moments using equations (A13) and (A14), after changing the residual velocities (c_ϖ, c_θ) for the dimensionless velocities referred to local values (ξ, η). We also used that $\mu_{100}^{(0)} = \mu_{010}^{(0)} = 0$.

$$
\begin{aligned}
V_\varpi = \mu_{100} &= \frac{m_*}{\sigma_*}\int\int\int c_\varpi \Psi \mathrm{d}c_\varpi \mathrm{d}c_\theta \mathrm{d}c_z \\
&= \frac{\sigma_*^0}{\sigma_*}\left[\frac{m_*}{\sigma_*^0}\int \mathrm{d}c_z \int\int c_\varpi \Psi_0 \mathrm{d}c_\varpi \mathrm{d}c_\theta - \frac{\vartheta_1}{\sigma_\varpi^2}\frac{m_*}{\sigma_*^0}\int \mathrm{d}c_z \int\int c_\varpi \Psi_0 (1-q)\,\mathrm{d}c_\varpi \mathrm{d}c_\theta\right] \\
&= -\frac{\sigma_*^0}{\sigma_*}\frac{\vartheta_1}{\sigma_\varpi^2}\frac{2\Omega(\varpi\Omega)}{\kappa}\langle\xi(1-q)\rangle = \frac{\sigma_*^0}{\sigma_*}\frac{\vartheta_1 K}{\kappa}\frac{\nu\pi}{\sin(\nu\pi)}\frac{1}{2\pi}\int_{-\pi}^{\pi}\sin(\nu\alpha)\sin\alpha\exp^{-\frac{a^2}{\mu_0}(1+\cos\alpha)}\mathrm{d}\alpha
\end{aligned}
\tag{A4}
$$

$$
V_\theta = \mu_{010} = \frac{m_*}{\sigma_*}\int\int\int c_\theta \Psi \mathrm{d}c_\varpi \mathrm{d}c_\theta \mathrm{d}c_z = -i\frac{\sigma_*^0}{\sigma_*}\frac{\vartheta_1 K}{2\Omega}\frac{\nu\pi}{\sin(\nu\pi)}\frac{1}{2\pi}\int_{-\pi}^{\pi}(1+\cos\alpha)\cos(\nu\alpha)\exp^{-\frac{a^2}{\mu_0}(1+\cos\alpha)}\mathrm{d}\alpha
\tag{A5}
$$

A3.3 Second-order moments

Here, we obtained the expressions for the second-order moments using equationa (A15), (A16) and (A17), after changing the residual velocities (c_ϖ, c_θ) for the dimensionless velocities referred to local values (ξ, η). We also used that $\mu_{110}^{(0)} = 0$ and $\mu_{020}^{(0)} = \mu_{200}^{(0)}(2\Omega/\kappa)^{-2}$.

$$
\begin{aligned}
\mu_{110} &= \frac{m_*}{\sigma_*}\int\int\int \Psi c_\theta c_\varpi \mathrm{d}c_\varpi \mathrm{d}c_\theta \mathrm{d}c_z = \frac{\sigma_*^0}{\sigma_*}\left(\mu_{110}^0 - \frac{\vartheta_1}{\sigma_\varpi^2}\frac{2\Omega}{\kappa}(\varpi\Omega)^2\langle\xi\eta(1-q)\rangle\right) \\
&= \frac{\sigma_*^0}{\sigma_*}\left(\frac{\vartheta_1\kappa}{2\Omega}\frac{a^2}{\mu_0}\frac{\nu\pi}{\sin(\nu\pi)}\frac{i}{2\pi}\int_{-\pi}^{\pi}\sin(\nu\alpha)\sin\alpha(1+\cos\alpha)\exp^{-\frac{a^2}{\mu_0}(1+\cos\alpha)}\mathrm{d}\alpha\right)
\end{aligned}
\tag{A6}
$$

$$
\begin{aligned}
\mu_{200} &= \frac{m_*}{\sigma_*}\int\int\int \Psi c_\varpi^2 \mathrm{d}c_\varpi \mathrm{d}c_\theta \mathrm{d}c_z = \frac{\sigma_*^0}{\sigma_*}\left(\mu_{200}^0 - \frac{\vartheta_1}{\sigma_\varpi^2}\left(\frac{2\Omega}{\kappa}\right)^2(\varpi\Omega)^2\langle\xi^2(1-q)\rangle\right) \\
&= \frac{\sigma_*^0}{\sigma_*}\left(\frac{\kappa}{2\Omega}\right)^2\left(\sigma_\varpi^2 - \vartheta_1\left[1 - \frac{\nu\pi}{\sin(\nu\pi)}\frac{1}{2\pi}\int_{-\pi}^{\pi}\left(1 - \frac{a^2}{\mu_0} - 2\frac{a^2}{\mu_0}\cos\alpha - \frac{a^2}{\mu_0}\cos^2\alpha\right)\cos(\nu\alpha)\exp^{-\frac{a^2}{\mu_0}(1+\cos\alpha)}\mathrm{d}\alpha\right]\right)
\end{aligned}
\tag{A7}
$$

$$
\begin{aligned}
\mu_{020} &= \frac{m_*}{\sigma_*}\int\int\int \Psi c_\theta^2 \mathrm{d}c_\varpi \mathrm{d}c_\theta \mathrm{d}c_z = \frac{\sigma_*^0}{\sigma_*}\left(\mu_{020}^0 - \frac{\vartheta_1}{\sigma_\varpi^2}(\varpi\Omega)^2\langle\eta^2(1-q)\rangle\right) \\
&= \frac{\sigma_*^0}{\sigma_*}\left(\frac{\kappa}{2\Omega}\right)^2\left(\sigma_\varpi^2 - \vartheta_1\left[1 - \frac{\nu\pi}{\sin(\nu\pi)}\frac{1}{2\pi}\int_{-\pi}^{\pi}\left(1 - \frac{a^2}{\mu_0} - 2\frac{a^2}{\mu_0}\cos\alpha - \frac{a^2}{\mu_0}\cos^2\alpha\right)\cos(\nu\alpha)\exp^{-\frac{a^2}{\mu_0}(1+\cos\alpha)}\mathrm{d}\alpha\right]\right)
\end{aligned}
\tag{A8}
$$

A3.4 Centered second-order moments

Expressions for the centred second-order moments have been obtained using the equations obtained in the previous sections (A2–A8).

$$
\begin{aligned}
\tilde{\mu}_{110} &= \frac{m_*}{\sigma_*}\int\int\int \Psi(c_\theta - V_\theta)(c_\varpi - V_\varpi)\mathrm{d}c_\varpi \mathrm{d}c_\theta \mathrm{d}c_z \\
&= \frac{m_*}{\sigma_*}\left(\int \mathrm{d}c_z \int\int \Psi c_\theta c_\varpi \mathrm{d}c_\varpi \mathrm{d}c_\theta - V_\theta \int \mathrm{d}c_z \int\int \Psi c_\varpi \mathrm{d}c_\varpi \mathrm{d}c_\theta - V_\varpi \int \mathrm{d}c_z \int\int \Psi c_\theta \mathrm{d}c_\varpi \mathrm{d}c_\theta + V_\theta V_\varpi \sigma_*\right) \\
&= \frac{\sigma_*^0}{\sigma_*}\left(\frac{\vartheta_1\kappa}{2\Omega}\frac{a^2}{\mu_0}\frac{\nu\pi}{\sin(\nu\pi)}\frac{i}{2\pi}\int_{-\pi}^{\pi}\sin(\nu\alpha)\sin\alpha(1+\cos\alpha)\exp^{-\frac{a^2}{\mu_0}(1+\cos\alpha)}\mathrm{d}\alpha - V_\theta V_\varpi \frac{\sigma_*}{\sigma_*^0}\right)
\end{aligned}
\tag{A9}
$$

$$
\begin{aligned}
\tilde{\mu}_{200} &= \frac{m_*}{\sigma_*} \int \int \int \Psi \, (c_\varpi - V_\varpi)^2 \, \mathrm{d}c_\varpi \, \mathrm{d}c_\theta \, \mathrm{d}c_z \\
&= \frac{m_*}{\sigma_*} \left(\int \mathrm{d}c_z \int \int \Psi c_\varpi^2 \, \mathrm{d}c_\varpi \, \mathrm{d}c_\theta + V_\varpi^2 \sigma_* - 2V_\varpi \int \mathrm{d}c_z \int \int \Psi c_\varpi \, \mathrm{d}c_\varpi \, \mathrm{d}c_\theta \right) \\
&= \frac{\sigma_*^0}{\sigma_*} \left(\sigma_\varpi^2 - \vartheta_1 \left[1 - \frac{\nu\pi}{\sin(\nu\pi)} \frac{1}{2\pi} \int_{-\pi}^{\pi} \left(1 - \frac{a^2}{\mu_0} \sin^2\alpha \right) \cos(\nu\alpha) \exp^{-\frac{a^2}{\mu_0}(1+\cos\alpha)} \mathrm{d}\alpha \right] - V_\varpi^2 \frac{\sigma_*}{\sigma_*^0} \right)
\end{aligned} \tag{A10}
$$

$$
\begin{aligned}
\tilde{\mu}_{020} &= \frac{m_*}{\sigma_*} \int \int \int \Psi \, (c_\theta - V_\theta)^2 \, \mathrm{d}c_\varpi \, \mathrm{d}c_\theta \, \mathrm{d}c_z \\
&= \frac{m_*}{\sigma_*} \left(\int \mathrm{d}c_z \int \int \Psi c_\theta^2 \, \mathrm{d}c_\varpi \, \mathrm{d}c_\theta + V_\theta^2 \sigma_* - 2V_\theta \int \mathrm{d}c_z \int \int \Psi c_\theta \, \mathrm{d}c_\varpi \, \mathrm{d}c_\theta \right) \\
&= \frac{\sigma_*^0}{\sigma_*} \left(\frac{\kappa}{2\Omega} \right)^2 \left(\sigma_\varpi^2 - \vartheta_1 \left[1 - \frac{\nu\pi}{\sin(\nu\pi)} \frac{1}{2\pi} \int_{-\pi}^{\pi} \left(1 - \frac{a^2}{\mu_0} - 2\frac{a^2}{\mu_0} \cos\alpha - \frac{a^2}{\mu_0} \cos^2\alpha \right) \cos(\nu\alpha) \exp^{-\frac{a^2}{\mu_0}(1+\cos\alpha)} \mathrm{d}\alpha \right] - V_\theta^2 \frac{\sigma_*}{\sigma_*^0} \right)
\end{aligned} \tag{A11}
$$

A3.5 Useful weighed averages with respect to Ψ_0

Next, we present some useful relations that can be easily obtained using the expression for the weighed averages with respect to Ψ_0 presented in Section A1, $\langle f \rangle$, and the Schwarzschild velocity distribution function (Ψ_0 in equation A1):

$$
\langle (1-q) \rangle = 1 - \frac{\nu\pi}{\sin(\nu\pi)} \frac{1}{2\pi} \int_{-\pi}^{\pi} \cos(\nu\alpha) \exp^{-\frac{a^2}{\mu_0}(1+\cos\alpha)} \mathrm{d}\alpha \tag{A12}
$$

$$
\langle \xi(1-q) \rangle = -\frac{a}{\mu_0} \frac{\nu\pi}{\sin(\nu\pi)} \frac{1}{2\pi} \int_{-\pi}^{\pi} \sin(\nu\alpha) \sin\alpha \exp^{-\frac{a^2}{\mu_0}(1+\cos\alpha)} \mathrm{d}\alpha \tag{A13}
$$

$$
\langle \eta(1-q) \rangle = \frac{ia}{\mu_0} \frac{\nu\pi}{\sin(\nu\pi)} \frac{1}{2\pi} \int_{-\pi}^{\pi} \cos(\nu\alpha) (1 + \cos\alpha) \exp^{-\frac{a^2}{\mu_0}(1+\cos\alpha)} \mathrm{d}\alpha \tag{A14}
$$

$$
\langle \xi^2(1-q) \rangle = \frac{\sigma_\varpi^2}{V_1^2} - \frac{1}{\mu_0} \frac{\nu\pi}{\sin(\nu\pi)} \frac{1}{2\pi} \int_{-\pi}^{\pi} \cos(\nu\alpha) \left(1 - \frac{a^2}{\mu_0} \sin^2\alpha \right) \exp^{-\frac{a^2}{\mu_0}(1+\cos\alpha)} \mathrm{d}\alpha \tag{A15}
$$

$$
\langle \eta^2(1-q) \rangle = \left(\frac{\kappa}{2\Omega} \right)^2 \frac{\sigma_\varpi^2}{(\varpi\Omega)^2} - \frac{1}{\mu_0} \frac{\nu\pi}{\sin(\nu\pi)} \frac{1}{2\pi} \int_{-\pi}^{\pi} \cos(\nu\alpha) \left(1 - \frac{a^2}{\mu_0} - 2\frac{a^2}{\mu_0} \cos\alpha - \frac{a^2}{\mu_0} \cos^2\alpha \right) \exp^{-\frac{a^2}{\mu_0}(1+\cos\alpha)} \mathrm{d}\alpha \tag{A16}
$$

$$
\langle \xi\eta(1-q) \rangle = -\frac{a^2}{\mu_0^2} \frac{\nu\pi}{\sin(\nu\pi)} \frac{i}{2\pi} \int_{-\pi}^{\pi} \sin(\nu\alpha) \sin\alpha (1 + \cos\alpha) \exp^{-\frac{a^2}{\mu_0}(1+\cos\alpha)} \mathrm{d}\alpha \tag{A17}
$$

A4 Analytical expression for vertex deviation

Using the expressions we obtained for the centred second-order moments (Section A3.4), we find the analytical formula for the l_v we present here.

$$
\frac{1}{2} \tan(2 \cdot l_v) = \frac{\tilde{\mu}_{110}}{\tilde{\mu}_{200} - \tilde{\mu}_{020}} = \frac{\frac{\mathrm{Re}(i\vartheta_1)}{\gamma} D_\nu^{(1)}(x) - V_\varpi V_\theta \frac{\sigma_*}{\sigma_*^0}}{\left(\sigma_\varpi^2 - \mathrm{Re}(\vartheta_1) \right) \left(1 - \frac{1}{\gamma^2} \right) + \mathrm{Re}(\vartheta_1) \left(D_\nu^{(2)} - \frac{D_\nu^{(3)}}{\gamma} \right) - \left(V_\varpi^2 - V_\theta^2 \right) \frac{\sigma_*}{\sigma_*^0}}, \tag{A18}
$$

where

$$
D_\nu^{(1)}(x) = x \frac{\nu\pi}{\sin(\nu\pi)} \frac{1}{2\pi} \int_{-\pi}^{\pi} \sin(\nu\alpha) \sin\alpha (1 + \cos\alpha) \exp^{-x(1+\cos\alpha)} \mathrm{d}\alpha
$$

$$
D_\nu^{(2)}(x) = \frac{\nu\pi}{\sin(\nu\pi)} \frac{1}{2\pi} \int_{-\pi}^{\pi} \cos(\nu\alpha) \left(1 - x \sin^2\alpha \right) \exp^{-x(1+\cos\alpha)} \mathrm{d}\alpha
$$

$$
D_\nu^{(3)}(x) = \frac{\nu\pi}{\sin(\nu\pi)} \frac{1}{2\pi} \int_{-\pi}^{\pi} \cos(\nu\alpha) \left(1 - x - 2x \cos\alpha - x \cos\alpha^2 \right) \exp^{-x(1+\cos\alpha)} \mathrm{d}\alpha
$$

This paper has been typeset from a TEX/LATEX file prepared by the author.